Energy & Environmental Science

ROYAL SOCIETY OF CHEMISTRY

PAPER

View Article Online
View Journal | View Issue

Cite this: *Energy Environ. Sci.*, 2023, **16**, 6155

Carbon photochemistry: towards a solar reverse boudouard refinery†

Camilo J. Viasus Pérez, *[ab] Juan Manuel Restrepo-Florez, [cd] Jessica Ye, [a] Nhat Truong Nguyen,[e] Athanasios A. Tountas,[a] Rui Song,[a] Chengliang Mao,[a] Andrew Wang,[a] Abdelaziz Gouda,[a] Samantha Corapi,[a] Shufang Ji,[a] Hamish MacLeod,[a] Jiaze Wu,[a] Alán Aspuru-Guzik,[ah] Christos T. Maravelias [fg] and Geoffrey A. Ozin ‡*[a]

Received 17th October 2022,
Accepted 7th November 2023

DOI: 10.1039/d2ee03353d

rsc.li/ees

Carbon and carbon dioxide can be concurrently converted using light to carbon monoxide *via* the reverse-Boudouard reaction. Nevertheless, the reaction's high endothermicity requires the reaction to be conducted at about 900 °C, which presents technical challenges associated with large-scale high-temperature energy-intensive operations. Herein, we demonstrate that the reverse-Boudouard reaction can be made practicable and profitable using sunlight in conjunction with light-emitting diodes, silicon photovoltaics, and lithium-ion batteries under room temperature conditions. The feasibility of this scheme is explored using a comparative technoeconomic analysis (TEA) to establish the viability of the process for converting several forms of carbonaceous waste and greenhouse gas carbon dioxide into a sustainable and value-added C1 feedstock, carbon monoxide.

Broader context

The light-powered reverse-Boudouard reaction converts carbon and carbon dioxide, a notorious greenhouse gas, into the industrially relevant C1 feedstock carbon monoxide, utilized in sectors such as metal fabrication, chemical synthesis, pharma and biotechnology, and electronics. The light-powered reverse-Boudouard reaction is less energetically and chemically intensive than the same reaction driven by heat. Furthermore, it supersedes current high-temperature processes, which produce toxic by-products and require fossil heat. Technological and economic feasibility analysis shows that the reverse Boudouard reaction enabled by sunlight, photovoltaics, light emitting diodes and lithium-ion batteries is industrially viable due to advancements in the efficiencies and cost of these renewable energy technologies. If successfully industrialized, the light-powered reverse Boudouard process can potentially displace fossil syngas and be considered as a platform for synthesizing sustainable chemicals and fuels.

[a] *Department of Chemistry, University of Toronto, Toronto, Ontario, ON, M5S 3H6, Canada. E-mail: g.ozin@utoronto.ca, cjviasusp@gmail.com*
[b] *Grupo de Investigación en Química de Coordinación y Bioinorgánica, Departamento de Química, Facultad de Ciencias, Universidad Nacional de Colombia, Av. Carrera 30 # 45-03, Sede Bogotá, Colombia*
[c] *Department of Chemical and Biological Engineering, University of Wisconsin-Madison, 1415 Engineering Dr, Madison, WI 53706, USA*
[d] *Department of Chemical Engineering, University of Florida, Gainesville, FL 32608, USA*
[e] *Department of Chemical and Material Engineering, Gina Cody School of Engineering and Computer Science, Concordia University, 1455 De Maisonneuve Blvd W, Montreal, Quebec H3G 1M8, Canada*
[f] *Department of Chemical and Biological Engineering, Princeton University, 50-70 Olden St, Princeton, NJ 08540, USA*
[g] *Andlinger Center For Energy and the Environment, 86 Olden St, Princeton, NJ 08540, USA*
[h] *Department of Computer Science, University of Toronto, Sandford Fleming Building, 10 King's College Road, Toronto, ON M5S 3G4, Canada*

† Electronic supplementary information (ESI) available. See DOI: https://doi.org/10.1039/d2ee03353d

‡ Lead contact.

Introduction

Fossil fuels continue to be the primary source of energy and feedstock chemicals for important industrial processes such as ammonia, methanol, olefin, and hydrogen production.[1–3] Currently, efforts are being made to transition towards more environmentally responsible alternatives. Carbon dioxide capture and utilization (CCU) for green fuels and feedstocks is a promising approach for combatting climate change.[4]

Carbon monoxide has been investigated as a choice CCU product with notable uses in metal fabrication and the chemicals industry.[4,5] Furthermore, when combined with hydrogen, the resulting syngas can be used in Fischer–Tropsch synthesis of hydrocarbon fuels.[6–8] Currently, the industrial production of syngas occurs *via* steam-methane reformation and/or coal or coke steam gasification, both of which are highly energy consuming and carbon footprint-intensive.[9]

Previous attempts at eco-friendly carbon monoxide production utilized thermal steam-gasification of fossil fuels, biomass, and/or waste materials, usually through auto-combustion of the carbonaceous feedstock.[10] Notably, the large-scale application of this technology is limited by high temperatures, ash melting, and tar contamination.[11] Also, thermal steam gasification generates a large carbon footprint, requires injections of pure oxygen, and produces combustion-related contaminants like dioxins and furans.[12,13] In comparison, the reverse-Boudouard reaction can be carried out under similar conditions to generate CO directly from CO_2 with limited harmful byproducts. Inconveniently, high thermal reaction enthalpies and temperatures greater than 900 °C (Fig. S1, ESI†) are required to effectively drive the reaction forward (eqn (1)).[14]

$$C + CO_2 \rightarrow 2CO \quad \Delta H^{\circ}_{298K} = +172\ \text{kJ mol}^{-1} \qquad (1)$$

While alkali, alkali-earth, and transition metal catalysts have been shown to somewhat decrease the reverse-Boudouard reaction temperature, reactor degradation from catalyst melting and deposition remains a concern.[15,16]

Herein, we experimentally demonstrate a room temperature light-driven reverse-Boudouard process and probe its feasibility for large-scale applications by conducting a comparative technoeconomic analysis using LED 24-7 *vs.* intermittent solar irradiance as light sources.

The results indicate that a continuous LED-based process is plausible and advances the design of photocatalytic processes for producing fuels and chemicals from carbon dioxide and various carbon sources.

Results and discussion

Ultraviolet-Visible (UV-Vis) spectroscopy (Fig. S2, ESI†), elemental analysis, powder X-ray diffraction (PXRD) (Fig. S3, ESI†), Raman spectroscopy (Fig. 1c), and X-ray photoelectron spectroscopy (XPS) (Fig. 1d and e) characterizations were conducted on two kinds of carbon black, one ultrapure and the other containing a low level of metal impurities (denoted ultrapure C_nB and C_nB CABOT, respectively) before and after light irradiation. Optical and infrared spectroscopy helped elucidate the structure, elemental composition, and presence of organic functionalities. Scanning and transmission electron microscopy (SEM and TEM) of C_nB CABOT showed that most carbon particles were smaller than 100 nm, consistent with literature reports on similar carbon black samples (Fig. 1a).[15] Raman spectroscopy analysis showed that sp^3 (single D band at $\sim$1350 cm^{-1}) and sp^2 (single G band at $\sim$1600 cm^{-1}) bands correspond to aromatic rings and carbon chain vibrations, respectively were the two diagnostic carbon stretching modes preserved following photoreaction. In addition, a noticeable D band enhancement was attributed to the formation of larger disordered carbon structures and defects induced by light irradiation. Following light irradiation, a higher amount of structural disorder associated with graphitic domains was noted as CO_2 consumes C_nB (I_D/I_G = 1.32 ± 0.06 before and 1.42 ± 0.05 after

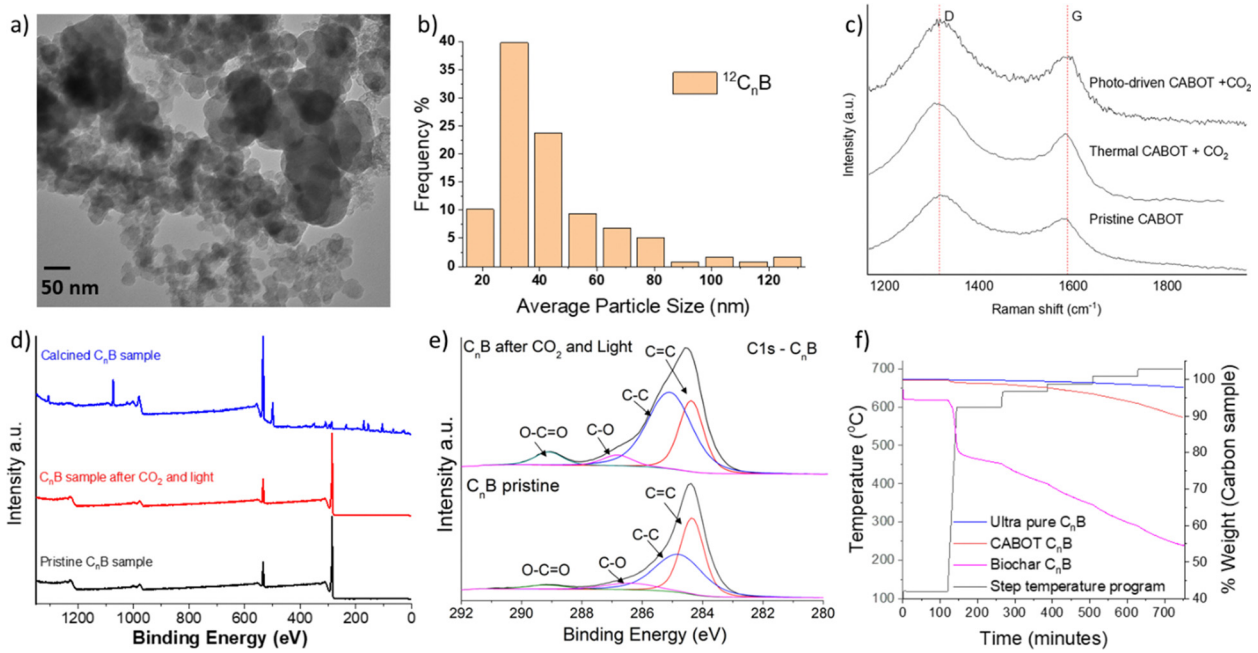

Fig. 1 (a) Transmission electron microscopy (TEM) image of the pristine C_nB CABOT sample; (b) particle size distribution of C_nB CABOT sample, (c) Raman spectroscopy of C_nB samples; (d) XPS survey of C_nB samples before (black line), after (red line) CO_2 and light, and air (blue line) calcined C_nB CABOT sample (169.4 ppm metal impurities) and (e) High-resolution C1s XPS analysis of C_nB CABOT sample before and after the photo-driven reverse-Boudouard reaction and (f) thermogravimetric analysis TGA step ramp on ultrapure C_nB, CABOT and Biochar samples. Xe lamp light intensity was set to 29 W cm^{-2} for samples in figure c (photo-driven CABOT CO_2), in d (red line) and in c after light and CO_2. Irradiation time and reactor pressure for c, d and e XPS analysis were 5 minutes and between 19–21 psig of CO_2 without appling external heat.

the photo-driven Boudouard reaction). This larger I_D/I_G ratio confirmed an increase in the degree of the generated disorder. A graphitic structural disorder, confirmed by the various intensity ratios of the D and G bands, was observed following the thermal treatment of the carbon black by TGA.

Analysis of ash residues from air combustion of C_nB at 600 °C, by TGA, ICP-MS and XPS (Fig. 1d) showed no detectable metal impurities. High-resolution C 1s XPS analysis showed that minor oxygenated functional groups on the pristine C_nB were enhanced as the reaction proceeds, confirming the oxidation of C_nB associated with the conversion of CO_2 to CO as well as the adsorption of minor amounts of CO_2 (Fig. 1e and Table S2-2, ESI†).

The TGA experiments performed on C_nB samples (ultrapure, CABOT and Biochar C_nB) in a CO_2 atmosphere demonstrated the influence of the metal impurities. In all cases, C_nB conversion rates (0.73–1.1 $mmol_{C_nB}$ cm^{-2} h^{-1} at 600 °C and 4.0–8.6 $mmol_{C_nB}$ cm^{-2} h^{-1} at 700 °C, respectively) and activation energies were consistent with literature reports for the thermally-driven reverse-Boudouard reaction.[14] The conversion of ultrapure, CABOT and biochar samples *via* $C_nB + CO_2 \rightarrow 2CO$ were shown to be thermodynamically favoured at temperatures above 600 °C, as seen in the step-ramped TGA (Fig. 1f). As expected, high activation energies were observed for this endothermic process (124.45 kJ mol^{-1} for the ultrapure C_nB and 150.1 kJ mol^{-1} for CABOT C_nB). The conversion follows the order Ultrapure Alfa Aesar < CABOT < Biochar confirming enhancements from metal impurities. Several reported studies on reverse Boudouard reactions using metals as catalysts showed improved CO rate and decreased apparent activation energies.[17–19]

Exploratory photo-driven reverse-Boudouard reactivity tests

Probe tests were performed using a 300 W Xe lamp (12.7 W cm^{-2} irradiation intensity, where 0.1 W cm^{-2} is equal to 1 sun) to select the optimal carbonaceous material (CM) for study (Fig. 2a).

Ultrapure C_nB black (made from acetylene by Alfa Aesar) and carbon nanotubes (Sigma-Aldrich) were found to be stable under CO_2 and light and presented low carbon monoxide production rates. Natural graphite samples were the most stable under light regardless of irradiation intensity or exposure time due to a lack of oxygenated functionalities and surface defects.[15] CABOT C_nB and biochar samples demonstrated the highest carbon monoxide production under light irradiation, matching the thermal reaction observations by TGA.[20,21] Though biochar showed the highest rates, CABOT C_nB was chosen for further study due its well-defined

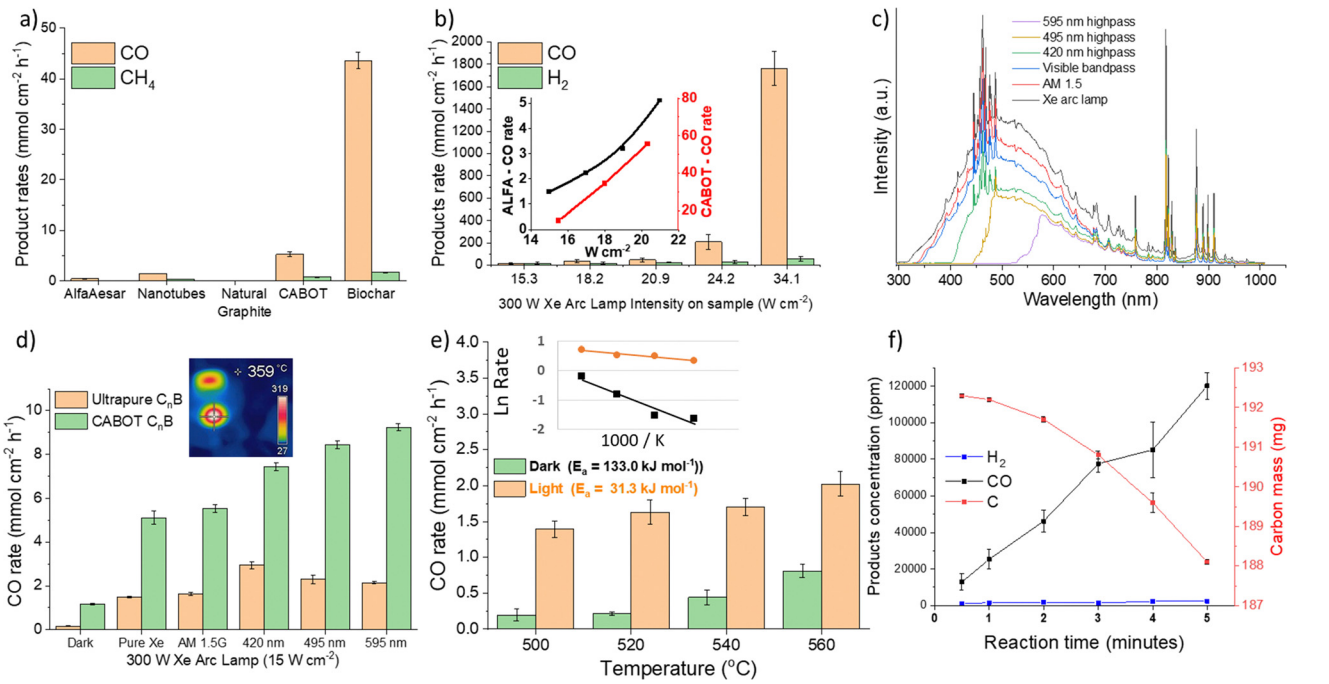

Fig. 2 (a) Photo-driven reverse-Boudouard reaction performed on several carbon sources with a Xe lamp at an irradiation intensity of 12.7 W cm^{-2}. (b) C_nB CABOT sample for power intensity studies. Photochemical behaviour was observed for CO production rates at intensities lower than 21 W cm^{-2} (R^2 = 0.998). The red line shows a linear rate increase using CABOT C_nB for the reverse-Boudouard reaction, while the black line shows an Arrhenius trend for ultrapure C_nB. (c) Simulated Xe light spectrum used for wavelength dependence studies. (d) Wavelength dependence studies with applied heating at 350 °C (to nullify the photothermal effect) and IR temperature measurement on ultrapure and CABOT C_nB samples at 15 W cm^{-2}. (e) Activation energies (E_a) in dark and light conditions for the temperature range of 500–560 °C using a photo-flow reactor; in each experiment, the total gas flow was set to 6 sccm (1 sccm CO_2: 5 sccm Ar) with an irradiated sample surface area of 0.126 cm^2; each sample weighed about 2–3 mg. LED simulated white light intensity used 4.8 W cm^{-2}. New samples were used for every test condition. (f) Kinetic experiments for the photothermal reverse-Boudouard reaction; Xe lamp light intensity was set to 34.1 W cm^{-2}. At least three individual measurements were used to calculate the error bars. Irradiation time and reactor pressure for a, b, d and f tests were 5 minutes and between 24–30 psig of CO_2 without external heat applied.

composition, size, structure, aggregation state, porosity, commercial availability and surface functionality.

Various light intensities were used to determine the photoresponsivity of CO production on CABOT C_nB and evaluate its photochemical and photothermal behaviour. These results are presented in Fig. 2b, where the rate graphs are linear below 21 W cm^{-2} and display Arrhenius behaviour at intensities above 21 W cm^{-2}. Although ultrapure C_nB showed an Arrhenius trend at irradiation intensities above 19 W cm^{-2}, it displayed a much lower CO production rate. These results demonstrated that the highly endothermic reverse-Boudouard process could be photochemically driven and suggests dominant photothermal contribution under high-intensity light and dominant photochemical behaviour at lower intensities below 21 W cm^{-2}. In addition, it showed that metal impurities, surface defects, C and O vacancies could dramatically increase the rate of CO production without interfering with the photochemical behaviour under low light intensities.

Influence of light intensity and wavelength dependence on the reverse-Boudouard reaction

To minimize photothermal effects under high-light intensity conditions and confirm the presence of photochemical contributions to the reverse-Boudouard process, a literature procedure using a fixed photon flux at the sample was followed.[22] The results at light intensities below 21 W cm^{-2} presented a linear correlation with CO formation rate, suggesting photochemical behaviour. Therefore we selected 15 W cm^{-2} for further tests to determine the role of light in CO_2 reduction over C_nB samples (Fig. 2d). An IR camera was used to measure the temperature generated on the sample surface under CO_2 in a photoreactor with a CaF_2 window. An unfiltered Xe-arc lamp set at the stated light intensity was used to heat the surface (Fig. 2d). The measured temperature was 350 °C due to the expectedly high optical absorption by a black carbon material (Fig. S2, ESI†). All systems were then heated to this temperature for subsequent experiments, where it is expected that any thermal contribution from the Xe lamp would become negligible. Bandpass filters (Fig. 2c) were used to evaluate the wavelength dependency of the reaction. Ultrapure and CABOT C_nB pellets (13 mm diameter and 2–3 mm thickness) were placed in a batch reactor and, after several vacuum/CO_2 purges, tested for photoactivity under CO_2 using the aforementioned conditions. The Xe lamp intensity was set to ensure all samples had an incident photon flux of 15 W cm^{-2} on the surface regardless of wavelength. The results are presented in Fig. 2d. Using unfiltered light from the Xe lamp, CO production rates of 1.5 and 5.3 mmol cm^{-2} h^{-1} for the ultra-pure and CABOT C_nB were observed, respectively.

To expand this comparison, rates of 0.16 (dark), 1.63, 2.93, 2.29, and 2.14 mmol cm^{-2} h^{-1} for ultrapure C_nB, and 1.16 (dark), 5.53, 7.43, 8.43, and 9.24 mmol cm^{-2} h^{-1} for CABOT C_nB were observed when highpass filters of AM 1.5G, 420, 495, and 595 nm were added, respectively (Fig. 2d). A linear increase in CO production rate was observed with each filter, confirming that photochemical behaviour varies with spectral wavelength range with CABOT C_nB, whereas the ultrapure C_nB sample presented a decreasing trend.[23] The unique photochemical behaviour of CABOT C_nB under irradiation for wavelengths higher than 595 nm for the highly endothermic reverse-Boudouard process was documented by irradiation with a Xe lamp at increasing intensities through the 595 nm highpass filter. It presented the highest activity towards CO, and the observed linear trend of the CO formation rate with the light intensity supports the photochemical contribution to the solar-driven reverse-Boudoaurd reaction (Fig. S4, ESI†).

In addition, we noted that minor amounts of molecular hydrogen were generated when irradiation intensities exceeded 15 W cm^{-2}. This was attributed to the dissociation of terminal CH moieties in carbon black and agreed well with the photochemical behaviour of H_2 generation presented in Fig. 2b.

Additional experiments evaluating the activation energies E_a of the reverse Boudouard process in the dark *vs.* light conditions were performed in a photo-flow reactor. First, we attempted to replicate the E_a observed by the TGA experiments. As presented in Fig. 2e, the light-assisted reactions yielded a dramatically lower E_a by four- to five-fold and increased the CO production rate compared to the dark process. This confirmed light's contribution to the process and suggested that the light-driven reaction likely proceeds through a different mechanism than the thermal reaction. The dark thermal results' similarity to those from TGA (E_a equal to 133.0 *vs.* 150.1 kJ mol^{-1} respectively) validated our reactor conditions, Fig. 1f and 2e.

Kinetic experiments

The following experiments were conducted assuming a non-equilibrium batch reactor system where the total conversion of CO_2 did not exceed 5%. The conditions presented in Fig. 2f, where the total CO_2 conversion fulfills this requirement, are not greater than 2% following up to 5 minutes of irradiation under a simulated solar light intensity of 34.1 W cm^{-2}. The kinetic rate expressions formulated in material S5 (ESI†) were associated with two separate reaction pathways. The first one corresponded to CO formation (photochemical behaviour in lower light intensity). The second was attributed to H_2 production from CH residues on the C_nB surface. Notably, H_2 production showed higher photochemical behaviour to increased light intensities than was seen for CO and deserves further study. Since the H_2 produced under these conditions was not significant compared to the CO from the reverse-Boudouard process, the rate law was expressed only as a function of CO_2 conversion, which depends only on the irradiated C_nB area and reaction time. As a result, the reaction order can be described by the following equation: $\mathrm{Ln}(r_A) = \mathrm{Ln}(k) + n\mathrm{Ln}(C_A)$ (material S5e1–e6, ESI†), where reaction order differences compared to the conventional thermal process were attributed to light effects.

LED wavelength dependence

Wavelength dependency tests were conducted using LEDs. UV-vis spectroscopy measurements (Fig. S2, ESI†) and the black nature of the material (band gap and sub-gap defect states see later) suggested that the selected carbon sample would absorb

strongly across a broad wavelength spectrum. In this context, we studied the wavelength dependence of the photo-driven reverse-Boudouard reaction using UV (365 nm), blue (470 nm), white (440–600 nm), green (525 nm), and red (625 nm) LEDs, the results of which are documented in Fig. S6 (ESI†). Linear photon flux-dependent CO production rates, with similar behaviour for the minor CH_4 co-product, were observed when the system was irradiated with UV light, suggesting photochemical behaviour (Fig. S6a, ESI†). CO production under blue LED light was found to follow Arrhenius behaviour, implying that blue wavelengths provide photothermal contributions to the solar-powered reverse-Boudouard reaction (Fig. S6b, ESI†), and was responsible for the photothermal activity shown in Fig. 2b at greater photon flux intensities. The green LED-driven reverse-Boudouard required intensities greater than 1.8 W cm^{-2} (Fig. S6c, ESI†) for product formation. At the same time, the white LED light showed irregular methane production rates with increased light intensity in addition to CO and minor ethylene and propylene co-production that increased linearly with light intensity (Fig. S6d, ESI†). Finally, the red LED showed a linear relationship between power intensity and CO formation rates and also produced minor amounts of methane and ethane (Fig. S6e, ESI†).

Red LEDs yielded the highest CO production rate, confirming the bandpass filter experiments using simulated solar light. As such, red LED light was used as the primary light source for subsequent experiments to compare to natural solar light irradiation experiments. To summarize, results from the individual LED experiments elucidated the source of each product observed during the photo-driven reverse-Boudouard reaction and the photochemical and photothermal contributions of specific wavelengths in the simulated and natural solar light process.

Natural solar reverse-Boudouard reaction

To confirm the photothermal effect or contribution, Photo-driven reverse-Boudouard experiments were conducted using natural sunlight on the roof of Lash Miller Laboratories to test reactivity under solar light as opposed to previous trials under simulated solar power from a Xe lamp. Several 13 mm diameter and 1–2 mm thick C_nB pellets were prepared by compressing the test material under two metric tonnes of pressure for 5 minutes using a commercial pellet press. The pellets were irradiated with natural sunlight focused to a 2–4 mm diameter spot using 7.5 cm and 12.7 cm diameter lenses in a CO_2 atmosphere. Typical unfocused natural solar light intensities ranged between 0.070–0.088 W cm^{-2}. Notably, Xe-arc lamps and natural sunlight have comparable spectra and photon fluxes (Fig. 2c and 3b); therefore, they are expected to produce comparable large-scale production rates.

To amplify our findings, irradiation with solar light at approximately 20 W cm^{-2} without external heating yielded higher CO production rates than the reported thermal process at 850 °C. Raising the incident light intensity to 43 W cm^{-2} yielded rates above those reported at 75 W of microwave radiation at 813 °C.[14] As expected, CO production rates increased with natural-light intensity, showing a linear trend characteristic of photochemical reaction pathways (Fig. 3a) or near photothermal-photochemical equilibrium due to the high conversion rate.

Notably, some low molecular weight unsaturated hydrocarbons were also observed, most likely from C_nB pyrolysis from visible wavelength contributions, as demonstrated in both the LED white and red wavelength experiments (Fig. S6d, ESI†). Overall, simulated solar Xe-arc lamp CO production rates agreed with those of natural solar experiments. A light-driven reverse-Boudouard process was proven to be accessible using sunlight. Thus, we experimentally demonstrated the feasibility of a solar-powered reverse Boudouard process.

Like with the Xe lamp simulated solar irradiation experiments, the use of solar irradiation through a 595 nm bandpass filter showed higher CO rates than the same intensity irradiation using the full spectrum, implying that the photo reverse-Boudouard process performance can be optimized by using mostly IR photon flux. The rate of formation and yield of CO agreed with the expected experiments conducted under natural light at intensities of 65 to 90 W cm^{-2} (Fig. 3a). This suggests that high-intensity LED systems could be employed to drive the reverse Boudouard process to overcome the intermittency of natural sunlight. Hence, experiments were conducted using high-intensity red LEDs (625 nm at 95 W cm^{-2}).

The wavelength dependence of the light-driven reverse-Boudouard reaction was also evaluated using 75 W cm^{-2} unfiltered solar light, UV, Visible and IR bandpass filters (Fig. 3c). The total irradiation power decreased from 75 to 62, 42, and 34 W cm^{-2} when the filters were used (Fig. 3c), yielding corresponding CO production rates of 3706, 1814, 161, and 176 mmol CO cm^{-2} h^{-1}, respectively. Wavelength variations using the light filters did not change which products were produced, though rates expectedly decreased with lower irradiation power.

Isotopic ^{13}C photo-driven reverse Boudouard reaction

Equal amounts of ^{12}CO and ^{13}CO were observed using isotopically labelled $^{13}CO_2$ over a CABOT $^{12}C_nB$ sample, establishing that carbon monoxide formed in equal amounts from each precursor thereby confirming the role of carbon dioxide in the reaction with natural solar irradiation (Fig. S7, ESI†).

Solar reverse Boudouard reaction pathway

A notable decrease in observed E_a for the reverse-Boudouard reaction in the light *versus* the dark (Fig. 2e), suggested that light is critical to the reaction progress. The thermal reaction was measured as a first-order reaction with Arrhenius behavior, as reported by the time-dependent weight loss experiments using carbon.[24] Typically, the thermally powered Boudouard reaction proceeds in two general steps where the first $C_nB_{(s)} + CO_{2(g)} \leftrightarrow C_nBO_{(s)} + CO_{(g)}$ eventually progresses to $C_nBO_{(s)} \rightarrow C_{n-1}B_{(s)} + CO_{(g)}$. This was confirmed experimentally by XPS analysis of post-reaction C_nB. Oxygenated functionalities were enhanced relative to the pre-reaction material, suggesting a

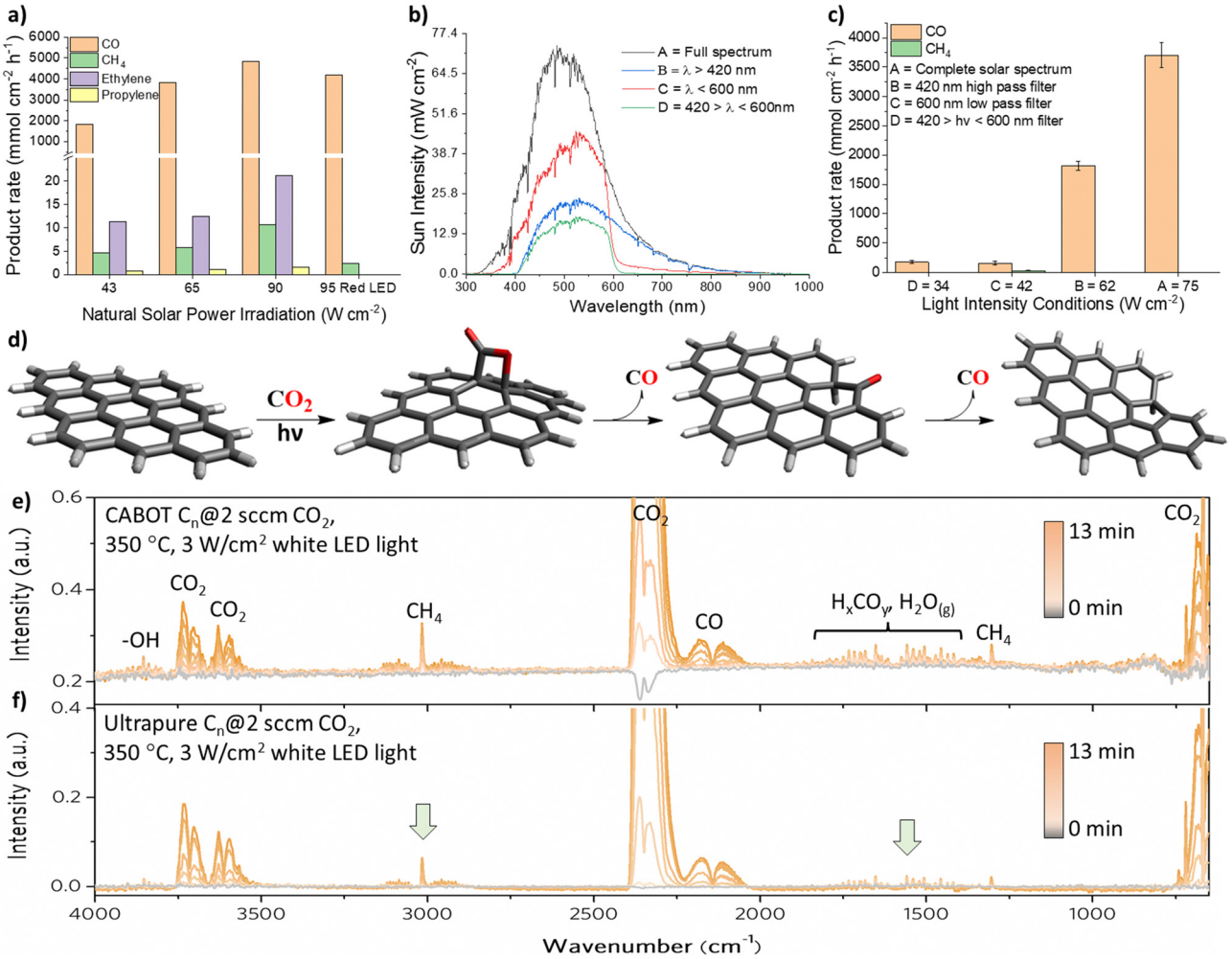

Fig. 3 (a) Rooftop natural solar irradiation and red LED tests on the reverse-Boudouard reaction at different light intensities. (b) Rooftop natural solar spectrum (A), with UV cut-off filter (B), IR cut-off filter (C), both C and B UV-IR cut-off filters (D). Light intensity change using several light filters. (d) DFT-based reaction pathway for the reverse-Boudouard reaction. (e) and (f) *In situ* DRIFTS experiments for CABOT and ultrapure carbon samples. Production rates following 10 minutes of irradiation in a batch reactor with CO_2 pressure of 15–20 psig. Minor and similar amounts of ethylene and propylene were observed in (c) but were not shown for clarity.

C_nBO moiety and C_nB–CO_2 adsorption-reaction intermediates following light irradiation (Fig. 1e).[25,26]

The carbon black C_nB used in this study has a high surface area (216 $m^2\ g^{-1}$) and strongly adsorbs CO_2 through hydrogen-bonding interactions with surface hydroxyl, carboxyl, and aromatic functionalities. The bound CO_2 is denoted by $C_nB\cdots CO_2$ (Fig. 3d and Fig. S8, ESI†). The ultra-black colour of the C_nB originates from intense broad absorptions across the entire solar spectrum, ranging from ultraviolet to visible wavelength polycyclic aromatic π to π* bandgap excitations and visible to near-infrared surface and defect related sub-gap excitations (eqn (2)–(5)).

Photoexcitation of the π to π* in C_nB's aromatic rings results in electron transfer to adsorbed CO_2, creating a charge-transfer surface intermediate as depicted in Fig. 3d:

$$C_nB\cdots CO_2 + h\nu \rightarrow (C_nB\cdots CO_2)^* \quad (2)$$

This process could disrupt the highly stable linear structure of CO_2, favouring a surface lactone species, enabling the elimination of CO, and promoting the formation of surface ketones or epoxides.

At surface edges, one could obtain surface ketones followed by the loss of the ketonic carbon,

$$(C_nB = O)^* \rightarrow C_{n-1}B + CO \quad (3)$$

resulting in the solar reverse-Boudouard reaction as the net reaction:

$$C_nB + CO_2 + h\nu \rightarrow C_{n-1}B + 2CO \quad (4)$$

On the other hand, for reactions directly on a surface plane, one could obtain a surface epoxide, followed by CO formation from the epoxidic carbon or the adsorption and cleavage of another CO_2 molecule near the surface epoxide, leading to the formation of oxygenated surface intermediates.

$$C_nB + CO_2 + h\nu \rightarrow C_n(O)_yB + CO \quad (5)$$

Fig. S10e (ESI†) illustrates a potential energetic landscape for intermediates involved in sequential CO_2 adsorption and CO

formation on a graphite surface model, as obtained through density functional theory (DFT) calculations. Importantly, it demonstrates that surface defects such as OH and substitutional O can involve intermediates more stable than that for a clean graphite surface, suggesting that carbon vacancy defects and electron-rich oxygenated species on the surface can help facilitate the photo-driven reverse Boudouard conversion of CO_2 to CO.

Non-radiative relaxation of the photogenerated aromatic π to π* bandgap electrons of the photoexcited states into sub-gap states denoted $(C_nB\cdots CO_2)^*$ could cause some local heating from a photothermal contribution to the reaction rate. However, this is envisioned to be a minor effect due to the order of magnitude difference between the activation energies of the light-driven (31.3 kJ mol^{-1}) and thermally-driven (133 kJ mol^{-1}) reverse-Boudouard reactions. The light-driven reaction is also dominated by a linear photochemical rate increase rather than an exponential Arrhenius rate increase with light intensity.

In situ diffuse reflectance infrared Fourier transform spectroscopy (DRIFTS) supported the proposed reaction scheme above (Fig. 3e). Two gaseous CO peaks (2075 and 2132 cm^{-1}) and two methane peaks (3016 and 1304 cm^{-1}) were observed after purging with 2 sccm of CO_2 through the CABOT C_nB sample. A peak corresponding to hydroxyl groups (3854 cm^{-1}) and multiplets (1329–1803 cm^{-1}) assigned to gaseous H_2O and chemically absorbed H_xCO_y species were observed.[27,28] These surface species increased with CO_2 concentration in the reaction chamber. Interestingly, the peak intensity ratio of H_2O-H_xCO_y/CO_2 increased sharply from 0.27 to 0.56 while the CO/CO_2 ratio remained constant and CH_4/CO_2 ratio decreased to 0.46 from 0.66 after altering the reaction condition from light to dark (Fig. 3e and f). These observations confirm the reaction between CABOT C_nB and CO_2 under light, with surface intermediates appearing to be carbonate or more complex (oxy)hydrocarbon compounds. These types of intermediates are also further supported by the results of structural relaxation calculations *via* DFT. Aside from CO production through the reverse Boudouard reaction, the generation of CH_4 and H_2O (or –OH) suggests side reactions involving C_nB-bonded hydrogen species, such as the reverse water gas shift and the Sabatier reactions. The light accelerated the transformation of H_xCO_y intermediates, removed surface-absorbed water, and facilitated CH_4 generation. Comparing the CABOT C_nB and ultrapure C_nB suggests that metal contaminants have higher CO production rates, higher CH_4-to-CO selectivity, and more H_2O–H_xCO_y intermediates on CABOT C_nB (Fig. 3f).

System-level analysis

Hereafter, we present the results of a technoeconomic analysis comparing two different Boudouard photocatalytic processes: a LED-based process (LED-P) consistent with the experimental approach used in this work and, based on the results obtained using a red LED, and an intermittently operating process (IO-P) using natural sunshine and buffered storage of intermediate products. Both processes intend to deal with the variability and intermittency of sunlight, one of the most challenging problems of sun-powered catalysis.[29,30] The LED process ensures uninterrupted operation by charging batteries during the day so that the LED-based reactor can be powered at night. The IO-P process relies on buffered storage of intermediate products, which can be consumed during the night so that the reactor does not operate at night but the rest of the plant remains in operation. We first describe the archetype processes and present techno-economic analyses for the base case designs. Then, we present a detailed sensitivity analysis and discuss the potential of these processes based on current projections for different technologies. We note that performing TEAs at low technology readiness levels (TRL 1–3) is crucial to identify a system's major cost drivers and helps guide future research paths such that the major cost drivers are addressed as the technology develops.[31] In fact, addressing design weaknesses is easy earlier in the design when there is more flexibility.

Archetype Boudouard processes

Fig. 4 presents the flowsheets corresponding to the two proposed processes. Fig. 4a shows the IO-P and Fig. 4b shows the LED-P. In both processes, excess CO_2, captured from a point source (not shown in the figure), and a CM (coal, biochar, *etc.*) are fed to the system. The CM is crushed and dried before feeding it to the reactor, where the Boudouard reaction (eqn (6)) occurs. This equation is a lumped representation of the main (Boudouard) and side reactions. We use lambda (λ) as a parameter to describe the selectivity toward CO.

$$CH_aO_b + \lambda CO_2 \rightarrow (2\lambda + b)CO + (1 - b - 2\lambda)CH_4 + \left(\frac{a}{2} - 2 + 2b + 4\lambda\right)H_2 + \lambda C \quad (6)$$

In addition to the formation of the main product (CO), methane, hydrogen and atomic carbon result as by-products (olefin formation is neglected). The CM is characterized by its moisture, ash, and elemental composition (nitrogen and sulphur are omitted for simplicity). Both in the IO-P and in the LED-P separation operations are identical: (1) a drying unit to remove moisture from the CM (2) a solid–gas separation system to recover unconverted carbon (cyclone); (3) a CO_2 capture system that enables recycling excess CO_2 (cryogenic distillation); and (4) a CO purification system (based on the COSORB technology) to remove the remaining by-products (see material S11 and S12 for details, ESI†). CO_2, unconverted CM, and atomic carbon are partially recycled to the reactor. The magnitude of the recycle streams is constrained such that a pre-established carbon : CO_2 ratio is maintained in the reactor, and the ash content at the reactor entrance does not surpass a pre-established limit.

In the IO-P, some units are shut down at night. Three buffer storage systems are required to keep the other units operational (Fig. 4a). Two of them store gas products. In contrast, the LED process uses batteries to store the required energy to operate the process at night (Fig. 4b). Although the IO-P and the LED-P rely on the same photocatalytic reaction, the reactor system varies significantly. In IO-P, we use parabolic collectors to

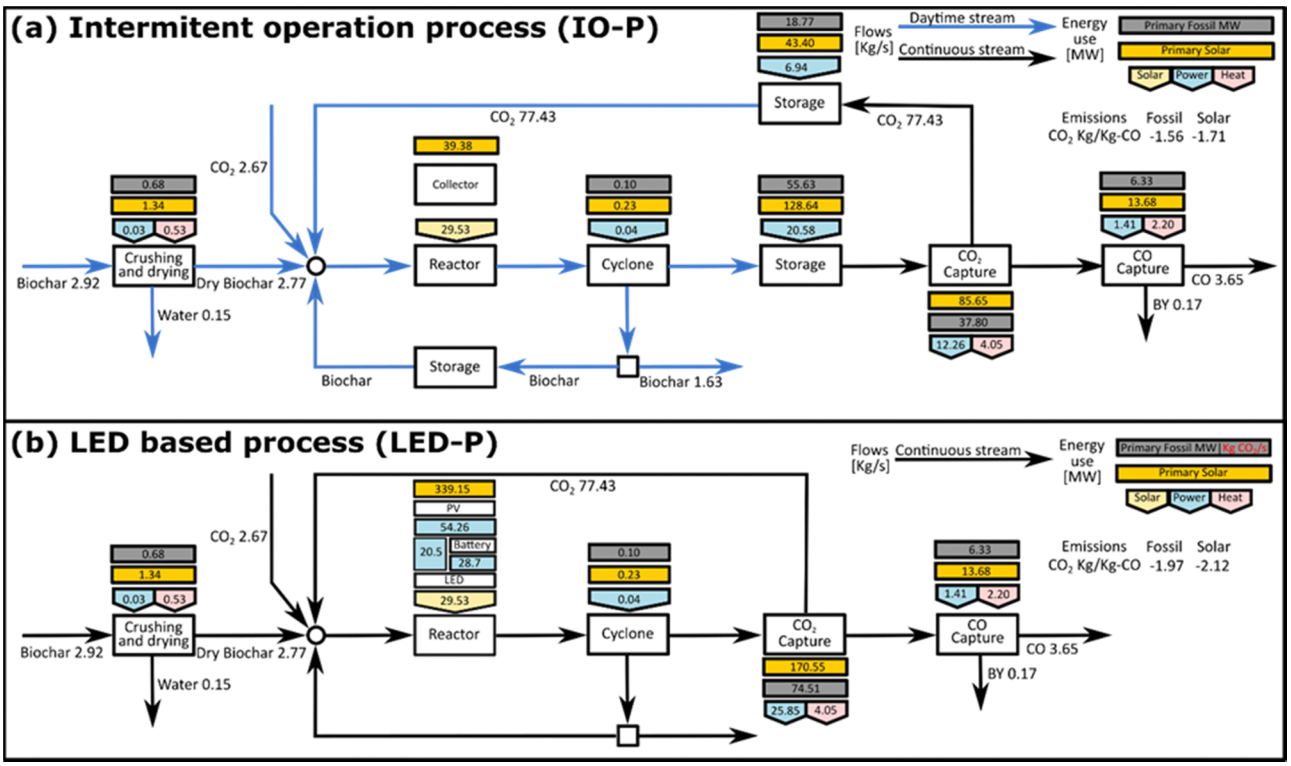

Fig. 4 Flowsheets of the archetype processes: (a) intermittent process (IO-P) (b) LED process (LED-P). Streams in blue are intermittent, while those in black operate continuously. Energy consumption in power, heat or direct irradiation is shown for the different units. Each unit's primary energy consumption is shown using dark yellow (solar) or grey (fossil) squares.

gather solar energy, whereas, in the LED-P, a photoreactor powered by an LED arrangement is used. We also consider using modular reactor units, where capacity can be added by increasing the number of reactor units rather than the size of the reactor.

We calculate the proposed processes' costs and study how different parameters affect their economics. To this end, we formulate a non-linear model (see material S11, ESI†), which consists of mass balances for the different operating units, equations to estimate their capital and operating costs, and a set of operational constraints (*e.g.*, the maximum ash content in reactor input, and excess CO_2). The model minimizes the minimum selling price (MSP) of CO. The solution yields, among others, component flows in all streams. Any CO_2 not recycled is captured and stored, while unconverted carbon that is not recycled is used for electricity generation and other energy-rich by-products (methane and hydrogen). The electricity generated offsets part of the process requirements. These processes are designed to remain operational during an average year's longest night (20 hours). The duration of this night is established based on results presented by Peng and Maravelias.[32] In the IO-P case, the ability to sustain operation through this longest night implies that the reactor and storage system are oversized based on this scenario; in contrast, we achieve this by oversizing the battery system in the LED-P case. In this work, we have relied on literature reports for the sizing and cost of different components of the designed system (reactor, collector, crushing and drying, and CO capture).[33–35] For other components (*e.g.*, cyclone and CO_2 capture), we relied on our own estimates based on detailed simulations using Aspen plus. (See material S12, ESI†).

Techno-economic analysis of the base case scenario

First, we compared the base case for the IO-P and the LED-P. Values for the most important model parameters are shown in Table 1. The values for these parameters have been estimated based on experiments reported in this work, state-of-the-art studies, or considering short-term projections. The parameters have been grouped into eight categories: chemistry (parameters associated with the reaction mechanism), operational (parameters describing reactor conditions), feedstock composition, feedstock costs, utilities cost, capital costs, and LED (used in LED-P only).

Biochar produced by the pyrolysis of lignocellulosic corn residues is selected as the CM (Elemental composition:[36] $CH_{0.4965}O_{0.087}$, ash content:[37] 5%, moisture content: 6.2%). We selected this CM due to its availability and sustainability. The results obtained, however, can be extrapolated to other types of CM. We note that the feedstock used here differs from the one used to characterize the reaction (*i.e.* CABOT C_nB).

However, biochar is expected to have greater reactivity than the studied system, presumably due to its higher metal content, and the results of this TEA should be treated as an underestimation of solar-powered reverse-Boudouard's potential.

The CO_2 feed was modelled to be obtained from a point source (*e.g.*, the fermentation outlet from an ethanol production plant), where it is captured; we assume that the

Table 1 Base case (Ref.), upper bound (UB) and lower bound (LB) values for the most relevant parameters in the model

Category	Parameter	Symbol	Units	LB	Ref.	UB	Source
Chemistry	Conversion	δ	%	10	20	40	Experiment
	Selectivity	ξ^{CO}	%	87.6	91	100	Experiment
	Light to chemical efficiency	η^{SCE}	%	20	30	80	38
Operational	Ash content in the reactor	λ^{Ash}	%	7	10	20	Assumed
	C|CO_2	$\lambda^{C\|CO_2}$	—	1 : 1	1 : 3	1 : 6	Experiment
Feedstock costs	CO_2	θ^{CO_2}	$$ per Ton	0	39.6	100	39
	CM	θ^{C}	$$ per Ton	100	300	500	40 and 41
Utilities	Electricity	θ^{E}	¢ per kW h	3	5.7	12	42
Capital costs	Separations	β^{S}	—	0.5×	1×	1×	Aspen plus,[43]
	Gast storage	β^{ST}	—	0.5×	1×	1×	Aspen plus
	Reactor	β^{R}	$$ per Module	1230	2460	4920	39
	Collector	β^{C}	$$ per Unit	13 300	26 600	53 200	39
LED	Power conversion efficiency	η^{PCE}	%	20	60	86	44
	Roundtrip efficiency	η^{BRE}	%	50	85	95	45
	Battery cost	θ^{BT}	$ per kW h	88	345	400	46

cost of CO_2 capture is 39.6 $ Ton^{-1}.[39] For the intermittent operation, we assume that at the location of the plant, the average solar irradiation is ~8.2 kW h m^{-2} (*e.g.*, in Southern California, near the city of Lancaster).[47] The dish system for solar energy collection is assumed to have 75% efficiency,[48] including optical losses and other inefficiencies.[34] Each dish is designed to collect 60.5 kW[34] and has an area of 88 m^2. Furthermore, we assume that the sun will be available for an average of 10 h per day. The capacity of the processes is such that ~80.000 Ton $year^{-1}$ of CO_2 is processed. We note that the overall solar to chemical efficiency based on the projected values is ~20%. This is an optimistic value but is consistent with other works in the field.[49]

We use typical efficiencies to calculate the primary energy requirements for converting fossil fuels or solar energy into electricity or heat.[50] The mass flows and energy requirements (divided into electricity, heat, and light) for the base cases are shown in Fig. 4. Except for the reactor, where solar energy is always used, these requirements can be satisfied using fossil fuels or solar energy as the primary source. The grey squares on top of each unit represent the primary energy consumption when fossil fuels are used. The dark yellow squares show the results when solar-derived utilities are employed. In what follows, we do not differentiate between the cost of solar and fossil-derived utilities, and we assume that the goal of parity between these two types of utilities has been achieved.

CO_2 emissions from cradle-to-gate were calculated for the LED-P and IO-P cases. These calculations were performed in GaBi (see material S16 for details, ESI†). The results obtained in kg-CO_2-eq per kg-CO are shown in Fig. 4. CO_2 emissions are significantly lower in the LED-P case (Fig. 4). The consumption of grid electricity in the IO-P, mainly used to compress gas streams, has a high environmental burden. In contrast, no compression is needed in the LED-P. Most of the electricity is consumed in the reactor, which is powered by photovoltaics and batteries; thus, the environmental impact is significantly reduced. For comparison, the emissions associated with CO production from synthesis gas are 0.626 kg-CO_2-eq per kg-CO. These values have been established based on the energy database in GaBi (see material S16.1 for more details, ESI†), and the energy consumption and yields for the biochar production have been set based on a system that uses corn stover feedstock.[51]

Economic metrics of the two base cases are shown in Fig. 5a presents how the MSP (US$ kg^{-1}), is distributed across five categories, while Fig. 5b shows the annualized capital and operating costs. For the base case, the LED-P leads to a lower MSP (US$ 2.63 kg^{-1} *versus* US$ 2.77 kg^{-1} for the IO-P). This difference can be attributed to the large capital cost associated with the overdesign in the IO-P case. For reference, attainable prices for CO using electrochemistry have been estimated between US$ 0.2–0.6 kg^{-1}.[52,53] The estimates are based on systems in which flue gas is used as the feedstock for carbon capture, typically using an amine-based process. The production of 1 mol of CO per mol CO_2 was assumed.[54] In these analyses, the major cost drivers are feedstock cost and electricity requirements. Comparing the cost of electrochemical CO_2 reduction with the estimate in our work, we conclude that significant technological improvements are still needed to achieve a cost similar to the reference technology. These results indicate that significant technological developments are still needed to achieve a cost similar to the reference technology. Furthermore, in Fig. S15 (ESI†), we show the price of syngas produced using the photocatalytic CO obtained in this work. We note that for the set of parameters used in the base case, the electricity stored in the LED process has approximately the same cost as the storage of gases plus the solar collector in the intermittent operation. The results presented are auspicious for LED-based photocatalytic technologies if we consider that the electricity storage costs are projected to decrease significantly in the coming decades[45,55] and that the efficiencies associated with the process may also increase. Furthermore, improvements in the modelling/design of equipment may lead to lower capital investments.[56]

Sensitivity analysis

In Fig. 6, we present a sensitivity analysis for the five different parameter groups. The ranges used in the sensitivity analysis have been selected to represent extreme points; that is, breakthrough improvements or significant underestimations of the

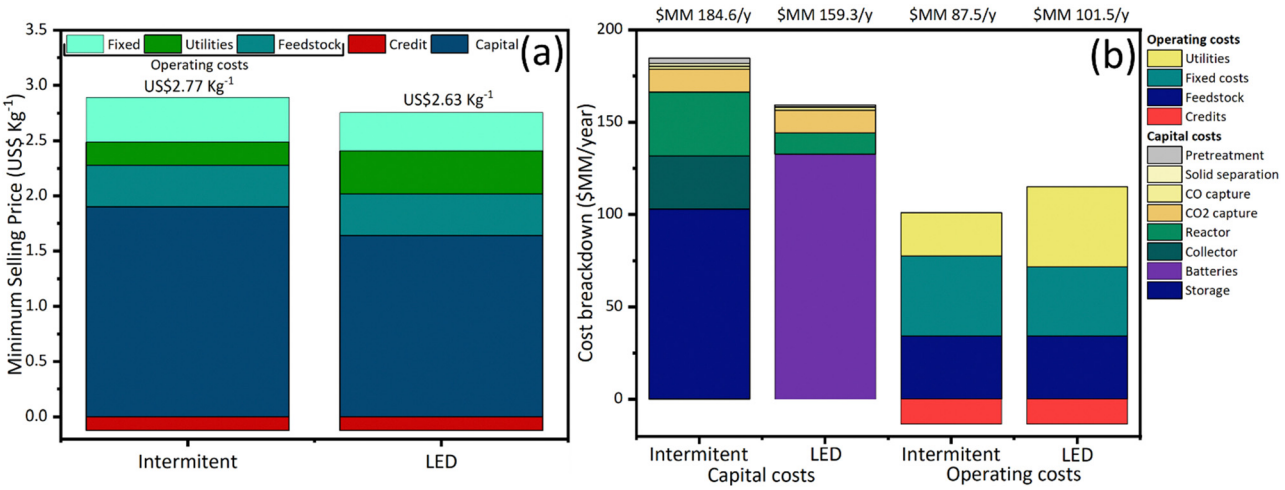

Fig. 5 Economics of the IO-P and the LED-P (a) breaking the minimum selling price (b) Annualized capital and operating costs.

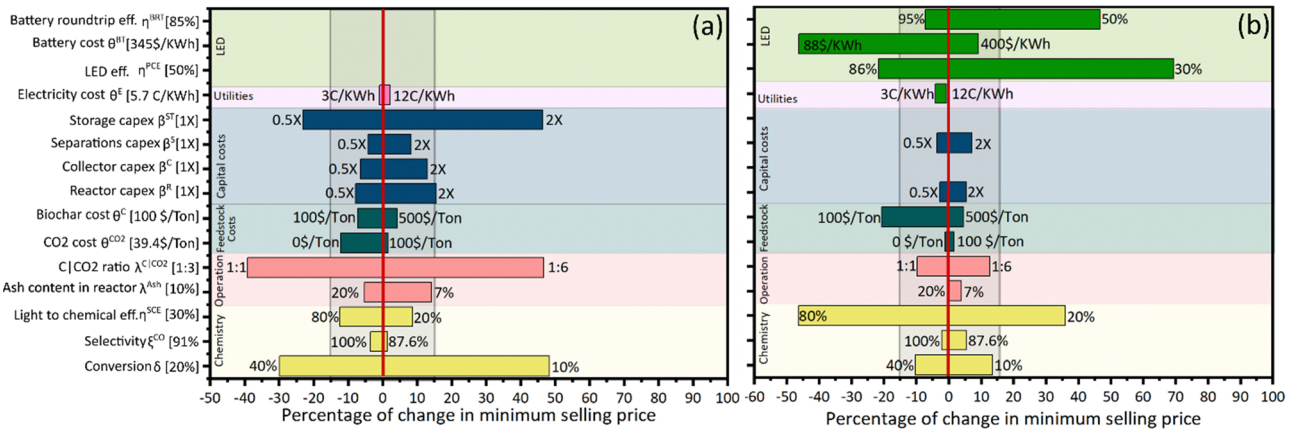

Fig. 6 Sensitivity analysis of the minimum selling price to changes in the parameters. (a) IO-P (b) LED-P. Values in brackets on the *y*-axis represent the reference value for the parameter (Table 1), while the values at the left and right sides of each bar correspond to the modified parameter value used in the sensitivity analysis. The *x*-axis represents the percentual change in the MSP with respect to the reference case when the parameter changes its value.

costs in comparison to the reference case. Fig. 6a shows the results for the IO-P, while Fig. 6b those for the LED-P. The shaded area encloses the region where ±15% changes in the MSP are obtained. Parameters with the largest effect on the MSP lead to changes outside this area. In the IO-P, the most important parameters are conversion (δ), the ash content in the reactor (λ^{Ash}), C|CO_2 fraction ($\lambda^{\mathrm{C|CO_2}}$), cost of CM ($\theta^{\mathrm{C}}$), and the capital cost of storage (β^{ST}). Among them, conversion, C|CO_2 fraction, and storage cost have the most significant impact. These three parameters are correlated, provided that the conversion and the C|CO_2 fraction determine the size of the gas storage units, which are responsible for a significant fraction of this system's capital and operating costs. In the LED-P, the most important parameters are: light to chemical efficiency (η^{SCE}), CM cost (θ^{C}), power conversion efficiency (η^{PCE}), and cost of storing electricity in the battery system (θ^{BT}). In this case, most of the variables are related to electricity consumption and storage, suggesting that advances in this field will be instrumental for the practical implementation of LED-P as a platform for photocatalysis.

We present a detailed sensitivity analysis using heat maps in Fig. S13-1–S13-3 (ESI†) to understand the importance of different parameters further. Additionally, in Fig. S14-1 (ESI†) we present a vision for the 2050 photocatalytic process showing the expected MSP when incremental improvements in the IO-P and LED-P parameters are implemented. The main conclusion from this analysis is that the IO-P and LED-P are similar in terms of achievable MSP in the medium and long term. The operational advantages of LED-P make them an attractive option. However, the economic viability of these processes is contingent upon the development of efficient and low-cost battery storage systems, photovoltaic conversion systems, and LEDs.

Conclusions

The potential technoeconomic relevance of a reverse-Boudouard reaction powered by light was evaluated by a system-level study that was undertaken to assess the feasibility

of using intermittent sunlight compared to continuous LED light for CO production. Compared to thermochemical and microwave reverse-Boudouard processes requiring temperatures greater than 900 °C, the solar-powered process operates with lower activation energy and without external heating. The photo-driven reverse-Boudouard reaction described herein details methods for converting different carbon sources and CO_2 into CO.

This brings one to the inescapable conclusion that the solar reverse-Boudouard process is technically feasible with advancements in battery efficiency, solar concentrators, and LEDs, together with their lower costs. Such a process would enable the production of CO from waste carbon and carbon dioxide and generate value-added feedstocks for a wide range of chemicals and chemical precursors.

Experimental

Materials

Carbon Black (C_nB) was purchased from CABOT (VULCAN XC72R GP-3921) and used as received. The material was found to have a surface area of 216 $m^2\ g^{-1}$. Carbon nanotubes, natural graphite, carbon black ($^{13}C_nB$) and carbon-^{13}C dioxide ($^{13}CO_2$ 99%) were purchased from Sigma-Aldrich and used as received. Ultrapure carbon black was purchased from AlfaAesar. Detailed characterization of as-received carbon black can be found in the ESI.† Before use, carbon dioxide (99.9% purity and purchased from Praxair) was passed through a dry alumina column. Carbon black samples were suspended in distilled water and placed in an ultrasound bath for 30 minutes before dropwise addition under vacuum onto glass fibre filters with a Pasteur pipette. After drying for 2 hours in a vacuum oven at 60 °C, the samples were exposed to simulated and natural solar light with and without external heat. For the natural solar tests, C_nB pellets were made with different diameters (4–13 mm) between 2–3 mm thickness and were prepared using a commercial pellet press at 2 metric tonnes for 5 minutes. Biochar was produced by slow pyrolysis of wood chips at 200 °C under N_2 atmosphere in a flow furnace for 6 hours. Then, the temperature was raised to 400 °C at 20 °C min^{-1} and maintained for 12 hours, during which the wood samples were monitored for pyrolysis completion. Depending on the size of the chips, the extra time and intermediate grinding were needed to ensure biochar formation.

Thermogravimetric analysis

TGA experiments were performed on a Discovery Series TGA from TA Instruments. A constant gas flow of 10 mL min^{-1} was used for a single-step ramp under N_2 and CO_2 over ^{12}CB CABOT, ^{12}CB AlfaAesar carbon black and Biochar samples and a gas flow of 20 mL min^{-1} was used for multiple-step ramps using only CO_2. Multiple isothermal step ramps were set at 20 °C intervals between 600 °C and 700 °C for 2 hours, each with a 20 °C min^{-1} ramp in between. In addition, CO_2 absorption measurements were performed on preheated samples in a CO_2 (20 mL min^{-1}) atmosphere at 120 °C to remove any dush and moisture impurities from the solid surface for 30 minutes, followed by a ramp of 30 °C min^{-1} up to 400 °C. The sample was then equilibrated until 60 °C and held isothermally for 10 min. During this step, the CO_2 is adsorbed on C_nB and was measured by a mass weight difference. Several cycles of the above procedure were performed to evaluate the stability of C_nB under CO_2 conditions and the amount of CO_2 absorbed and thermally desorbed.

Characterizations

PXRD patterns were collected on a Bruker D2-Phaser X-ray diffractometer using Cu Kα radiation at 30 kV. Diffuse reflectance spectra were collected using a Lambda 1050 UV/vis/NIR PerkinElmer spectrometer with an integrating sphere. As-received and post-reaction carbon black XPS were performed on a Thermo Scientific Kα with an Al Kα X-ray source. SEM and TEM were done using a Hitachi S-5200 HRSEM and JEOL 2010 HRTEM, respectively. Raman spectrums from 875 to 1950 cm^{-1} wavenumbers were collected on a CABOT pellet (10 mm diameter spot irradiated area) before and after the photo-driven Boudouard process and after TGA analysis at 640 °C under CO_2 atmosphere for two hours using a red laser (785 nm) in a Bruker Senterra Raman microscope at 1 mW of power. At least three different spots were analyzed over 60 seconds of exposure time (Fig. 1c).

The amounts of $^{12}CO/^{13}CO$ produced were analyzed using a GCMS spectrometer (Agilent 7890B-5977A MSD, using He as carrier gas) equipped with an automated injection gas sampling valve over three capillary columns (Molsieve, HP-PLOT/Q + PT and DB-FFAP) to improve separation and quantification. Reactions carried out in a batch reactor used an average sample mass of ~0.3 to 1.1 mg and deposited on borosilicate filters. Alternatively, pellets of 13 mm diameter were placed in a reactor equipped with a quartz window and pressurized with 24 to 30 psi of CO_2. Natural solar light irradiated the samples with a measured intensity between 20–90 W cm^{-2} for 10 minutes. A 300 W Xe arc lamp from PerfectLight company was used to simulate the sun during the preliminary and wavelength experiments (Fig. S9, ESI†). Following this, LED measurements were conducted by a flame ionization detector (FID) on an SRI8610 GC instrument. *In situ* DRIFTS spectrums were collected on a Thermo Scientific iS50 Fourier transform infrared (FT-IR) with a liquid nitrogen-cooled MCT detector. 32 or 64 spectra were co-added with a resolution of 4 cm^{-1}. The carbon powders were placed into a Harrick reaction chamber holder, ramped to 350 °C, and held for 2 h to remove adsorbed water and organic contaminants under 2 sccm H_2 flow. Subsequently, the carbon sample was held at 350 °C for 5 min under 10 W white LED irradiation to obtain stable background spectra after the H_2 flow rate was attenuated to 0. Finally, 2 sccm CO_2 flow was introduced and the *in situ* CO_2 reduction DRIFTS spectra were recorded with time.

Author contributions

C. J. V. P. and G. A. O. conceived the idea, designed all experiments and co-wrote the manuscript. C. J. V. performed

photochemical testing (natural, LED and simulated solar light tests), Raman, XPS, XRD and Kinetics experiments. J. M. R. F. and C. T. M. performed the system level and technoeconomic analysis and co-wrote the manuscript. J. Y., N. T. N., A. A. T., R. S., J. W., A. G., S. J., S. C. and C. M. performed the analytical characterization methods DRIFT, XRD, TEM, XPS, Raman and experimental testing. A. W. and A. A. G. performed the DFT calculations. All authors discussed the results and commented on the manuscript.

Conflicts of interest

There are no conflicts to declare.

Acknowledgements

G. A. O. thanks the University of Toronto, the Natural Sciences and Engineering Council of Canada, and Hydrofuel Inc. for supporting this research. N. T. N. acknowledges financial support from NSERC and Concordia University. C. J. V. P. wants to thank especially John Ford, Ahmed Bobat and David Heath from the machine shop at the University of Toronto for the fantastic work building the photochemical reactors and holders for the focusing lenses used in this project.

References

1 R. Dittmeyer, M. Klumpp, P. Kant and G. Ozin, *Nat. Commun.*, 2019, **10**, 1–8.
2 D. Welsby, J. Price, S. Pye and P. Ekins, *Nature*, 2021, **597**, 230–234.
3 J. Raza, A. H. Khoja, M. Anwar, F. Saleem, S. R. Naqvi, R. Liaquat, M. Hassan, R. Javaid, U. Y. Qazi and B. Lumbers, *Renewable Sustainable Energy Rev.*, 2022, **168**, 112774.
4 P. Voßnacker, A. Wüst, T. Keilhack, C. Müller, S. Steinhauer, H. Beckers, S. Yogendra, Y. Schiesser, R. Weber, M. Reimann, R. Müller, M. Kaupp and S. Riedel, *Sci. Adv.*, 2021, **7**, 5186–5215.
5 L. Wang, M. Ghoussoub, H. Wang, Y. Shao, W. Sun, A. A. Tountas, T. E. Wood, H. Li, J. Y. Y. Loh, Y. Dong, M. Xia, Y. Li, S. Wang, J. Jia, C. Qiu, C. Qian, N. P. Kherani, L. He, X. Zhang and G. A. Ozin, *Joule*, 2018, **2**, 1369–1381.
6 M. Fiore, V. Magi and A. Viggiano, *Appl. Energy*, 2020, **276**, 115415.
7 K. W. Jun, H. S. Roh, K. S. Kim, J. S. Ryu and K. W. Lee, *Appl. Catal., A*, 2004, **259**, 221–226.
8 A. A. Tountas, G. A. Ozin and M. M. Sain, *Nat. Catal.*, 2021, **4**, 934–942.
9 X. Yang and L. Ge, *Adv. Bioenergy*, 2017, 125–188.
10 T. Melchior, C. Perkins, P. Lichty, A. W. Weimer and A. Steinfeld, *Chem. Eng. Process.*, 2009, **48**, 1279–1287.
11 M. Asadullah, *Renewable Sustainable Energy Rev.*, 2014, **29**, 201–215.
12 P. v Zedtwitz and A. Steinfeld, *Energy*, 2003, **28**, 441–456.
13 N. Piatkowski, C. Wieckert, A. W. Weimer and A. Steinfeld, *Energy Environ. Sci.*, 2011, **4**, 73–82.
14 J. Hunt, A. Ferrari, A. Lita, M. Crosswhite, B. Ashley and A. E. Stiegman, *J. Phys. Chem. C*, 2013, **117**, 26871–26880.
15 P. Lahijani, Z. A. Zainal, M. Mohammadi and A. R. Mohamed, *Renewable Sustainable Energy Rev.*, 2015, **41**, 615–632.
16 C. Wang, W.-C. D. Yang, D. Raciti, A. Bruma, R. Marx, A. Agrawal and R. Sharma, *Nat. Mater.*, 2021, **20**, 346–352.
17 B. Yang, R. Ran, Y. Zhong, C. Su, M. O. Tadé and Z. Shao, *Angew. Chem., Int. Ed.*, 2015, **54**, 3722–3725.
18 Y. Jiao, W. Tian, H. Chen, H. Shi, B. Yang, C. Li, Z. Shao, Z. Zhu and S.-D. Li, *Appl. Energy*, 2015, **141**, 200–208.
19 S. C. Pereira, M. F. Ribeiro, N. Batalha and M. M. Pereira, *Greenhouse Gases: Sci. Technol.*, 2017, **7**, 843–851.
20 V. Hadiya, K. Popat, S. Vyas, S. Varjani, M. Vithanage, V. Kumar Gupta, A. Núñez Delgado, Y. Zhou, P. Loke Show, M. Bilal, Z. Zhang, M. Sillanpää, S. Sabyasachi Mohanty and Z. Patel, *Bioresour. Technol.*, 2022, **355**, 127303.
21 K. Xu, S. Hu, S. Su, C. Xu, L. Sun, C. Shuai, L. Jiang and J. Xiang, *Energy Fuels*, 2012, **27**, 118–125.
22 P. G. O'Brien, A. Sandhel, T. E. Wood, A. A. Jelle, L. B. Hoch, D. D. Perovic, C. A. Mims and G. A. Ozin, *Adv. Sci.*, 2014, **1**, 1400001.
23 G. Baffou, I. Bordacchini, A. Baldi and R. Quidant, *Light: Sci. Appl.*, 2020, **9**, 108.
24 C.-C. Chen, T. Maruyama, P.-H. Hsieh and J. R. Selman, *ECS*, 2010, 227–239.
25 C. J. Viasus, N. P. Alderman, S. Licciulli, I. Korobkov and S. Gambarotta, *Chem. – Eur. J.*, 2017, **23**, 17269–17278.
26 C. J. Viasus, B. Gabidullin and S. Gambarotta, *Angew. Chem., Int. Ed.*, 2019, **58**, 14887–14890.
27 T. H. Tan, B. Xie, Y. H. Ng, S. F. B. Abdullah, H. Y. M. Tang, N. Bedford, R. A. Taylor, K.-F. Aguey-Zinsou, R. Amal and J. Scott, *Nat Catal*, 2020, **3**, 1034–1043.
28 D. Li, F. Xu, X. Tang, S. Dai, T. Pu, X. Liu, P. Tian, F. Xuan, Z. Xu, I. E. Wachs and M. Zhu, *Nat Catal*, 2022, **5**, 99–108.
29 E. Schroeder and P. Christopher, *ACS Energy Lett.*, 2022, 880–884.
30 X. Peng, T. W. Root and C. T. Maravelias, *AIChE J.*, 2019, **65**, 10–16.
31 K. Roh, A. Bardow, A. Bardow, A. Bardow, A. Bardow, D. Bongartz, J. Burre, W. Chung, S. Deutz, D. Han, M. Heßelmann, Y. Kohlhaas, A. König, J. S. Lee, R. Meys, S. Völker, M. Wessling, J. H. Lee, A. Mitsos, A. Mitsos and A. Mitsos, *Green Chem.*, 2020, **22**, 3842–3859.
32 X. Peng, T. W. Root and C. T. Maravelias, *AIChE J.*, 2019, **65**, 10–16.
33 S. V. Jangam, M. Karthikeyan and A. S. Mujumdar, *Drying Technol.*, 2011, **29**, 395–407.
34 J. Kim, J. E. Miller, C. T. Maravelias and E. B. Stechel, *Appl. Energy*, 2013, **111**, 1089–1098.
35 Y. Il Lim, J. Choi, H. M. Moon and G. H. Kim, *Korean Chem. Eng. Res.*, 2016, **54**, 320–331.
36 C. Qian, Q. Li, Z. Zhang, X. Wang, J. Hu and W. Cao, *Fuel*, 2020, **265**, 116925.

37 C. Qian, Q. Li, Z. Zhang, X. Wang, J. Hu and W. Cao, *Fuel*, 2020, **265**, 116925.
38 J. Kim, T. A. Johnson, J. E. Miller, E. B. Stechel and C. T. Maravelias, *Energy Environ. Sci.*, 2012, **5**, 8417–8429.
39 J. Kim, T. A. Johnson, J. E. Miller, E. B. Stechel and C. T. Maravelias, *Energy Environ. Sci.*, 2012, **5**, 8417–8429.
40 I. Takahashi, *Sen'i Gakkaishi*, 1952, **8**, 163–164.
41 S. Shabangu, D. Woolf, E. M. Fisher, L. T. Angenent and J. Lehmann, *Fuel*, 2014, **117**, 742–748.
42 D. Humbird, R. Davis, L. Tao, C. Kinchin, D. Hsu, A. Aden, P. Schoen, J. Lukas, B. Olthof, M. Worley, D. Sexton and D. Dudgeon, *Process Design and Economics for Biochemical Conversion of Lignocellulosic Biomass to Ethanol: Dilute-Acid Pretreatment and Enzymatic Hydrolysis of Corn Stover*, Golden, CO (United States), Colorado, 2011.
43 Y. Il Lim, J. Choi, H. M. Moon and G. H. Kim, *Korean Chem. Eng. Res.*, 2016, **54**, 320–331.
44 P. Morgan Pattison, M. Hansen and J. Y. Tsao, *LED lighting efficacy: Status and directions*, Albuquerque, 2018.
45 W. Cole, A. W. Frazier, W. Cole and A. W. Frazier, *Cost Projections for Utility-Scale Battery Storage: 2020 Update*, 2020.
46 W. Cole, A. W. Frazier and C. Augistine, *National Renewable Energy Laboratory (NREL)*, 2021, p. 21.
47 Solar Atlas.
48 C. Kutscher, F. Burkholder and J. Kathleen Stynes, *J. Solar Energy Eng., Trans. ASME*, 2012, **134**(1), 011012.
49 J. Kim, C. A. Henao, T. A. Johnson, D. E. Dedrick, J. E. Miller, E. B. Stechel and C. T. Maravelias, *Energy Environ. Sci.*, 2011, **4**, 3122.
50 A. A. Tountas, X. Peng, A. V. Tavasoli, P. N. Duchesne, T. L. Dingle, Y. Dong, L. Hurtado, A. Mohan, W. Sun, U. Ulmer, L. Wang, T. E. Wood, C. T. Maravelias, M. M. Sain and G. A. Ozin, *Adv. Sci.*, 2019, **6**, 1801903.
51 K. G. Roberts, B. A. Gloy, S. Joseph, N. R. Scott and J. Lehmann, *Environ. Sci. Technol.*, 2010, **44**, 827–833.
52 O. S. Bushuyev, P. De Luna, C. T. Dinh, L. Tao, G. Saur, J. van de Lagemaat, S. O. Kelley and E. H. Sargent, *Joule*, 2018, **2**, 825–832.
53 A. Somoza-Tornos, O. J. Guerra, A. M. Crow, W. A. Smith and B. M. Hodge, *iScience*, 2021, **24**(7), 102813.
54 J. A. Herron, J. Kim, A. A. Upadhye, G. W. Huber and C. T. Maravelias, *Energy Environ. Sci.*, 2014, **8**, 126–157.
55 U.S. Department of Energy, *The SunShot 2030*, 2017.
56 E. Kayahan, M. Jacobs, L. Braeken, L. C. J. Thomassen, S. Kuhn, T. Van Gerven and M. E. Leblebici, *Beilstein J. Org. Chem.*, 2020, **16**, 2484–2504.